Ultrahigh-Resolution Optoelectronic Vector Analysis Utilizing Photonics-Based Frequency Up- and Down-Conversions

Min Xue, Minghui Lv, Qi Wang, Changyuan Yu, and Shilong Pan, *Senior Member, IEEE, Fellow, OSA*

***Abstract*—An ultrahigh-resolution optoelectronic vector analyzer (OEVA) to characterize optoelectronic (O/E) frequency responses of photodetectors is proposed and experimentally demonstrated, which is characterized by potential sub-Hz frequency resolution, doubled frequency range and large dynamic range. A carrier-suppressed optical double-sideband (ODSB) signal generated by modulating two frequency-swept RF signals with a fixed frequency spacing is used as a probe signal, which is then converted into a photocurrent by the photodetector (PD) under test. Comparing the frequency up- and down-conversion components in the generated photocurrent, the O/E frequency responses can be achieved with no need to know the response of the electro-optic modulator and the modulation indices. As the desired components achieved by frequency up- and down-conversion are frequency distinguished from the two RF signals, the proposed OEVA is immune to electromagnetic interference during on-chip measurement. In the experiment, the O/E frequency responses of two high-speed PDs are characterized from 0.1 to 67 GHz using a 25-GHz Mach-Zehnder modulator (MZM). The frequency resolution is up to 200 kHz. Additionally, the measurement error analysis is analyzed, and the noise performance and the dynamic range are experimentally investigated and discussed.**

***Index Terms*—Optoelectronic measurement, optical variables measurement, measurement techniques, microwave photonics.**

Manuscript received December 21, 2019; revised February 25, 2020; accepted March 17, 2020. Date of publication March 19, 2020; date of current version July 23, 2020. This work was supported in part by the National Natural Science Foundation of China under Grant 61705103 and Grant 61527820, in part by the National Key R&D Program of China under Grant 2017YFF0106900, in part by the Hong Kong Scholar Program (G-YZ2S), in part by the Jiangsu Provincial Program for High-level Talents in Six Areas (DZXX-034), and in part by Fundamental Research Funds for the Central Universities under Grants NC2018005. *(Corresponding authors: Shilong Pan).*

Min Xue is with the Key Laboratory of Radar Imaging and Microwave Photonics, Ministry of Education, the Nanjing University of Aeronautics and Astronautics, Nanjing 210016, China, and also with the Department of Electronic and Information Engineering, Hong Kong Polytechnic University, Kowloon, Hong Kong.

Minghui Lv, Qi Wang, and Shilong Pan are with the Key Laboratory of Radar Imaging and Microwave Photonics, Ministry of Education, the Nanjing University of Aeronautics and Astronautics, Nanjing 210016, China (e-mail: lllminghui@nuaa.edu.cn; wangqi_0207@nuaa.edu.cn; pans@nuaa.edu.cn).

Changyuan Yu is with the Department of Electronic and Information Engineering, Hong Kong Polytechnic University, Kowloon, Hong Kong (e-mail: changyuan.yu@polyu.edu.hk).

Color versions of one or more of the figures in this article are available online at http://ieeexplore.ieee.org.

Digital Object Identifier 10.1109/JLT.2020.2982066

I. Introduction

MICROWAVE photonics (MWP) is attractive owing to the capability of manipulating ultra-wide spectrum with ultrahigh frequency resolution [1]–[3], which enables lots of emerging applications, such as 5th generation (5G) mobile communication [4], precise optical sensing [5], ultrahigh-resolution radar imaging [6] and high-performance instrumentation [7]. Photodetectors (PDs), which are used to perform optical-to-electrical conversions, are fundamental devices in the MWP-based applications. Their frequency responses are very important for high-performance MWP systems.

To measure the optoelectronic (O/E) frequency responses, great efforts have been devoted and numerous methods have been developed, among which the all-optical methods, namely the optical spectrum method [8]–[14] and the optical heterodyne method [15]–[17], are the most widely used ones. The two methods generally have a wide measurement range but suffer from relatively low-frequency resolution. For MWP-based applications, ultrahigh-resolution O/E frequency response measurement is essential and highly desired. To achieve the ultrahigh-resolution measurement, one promising solution is to use the harmonic analysis method [18]–[20] or the electrical spectrum analysis method [21]–[24], by which a sub-Hertz resolution is potentially achievable. The harmonic analysis method has a doubled frequency range by detecting the second harmonic component in the generated photocurrent. However, to achieve the precise measurement, an electro-optic modulator (EOM) with high extinction ratio (ER) is required to well suppress the undesired sidebands. In the electrical spectrum analysis method, complicated electro-optic modulation (e.g., the two-stage modulation) places a restriction on the signal-to-noise ratios (SNRs) of the desired sidebands, which eventually results in a small dynamic range. Recently, by employing the two-tone modulated signal, the measurement accuracy together with the dynamic range of the electrical spectrum analysis method is greatly improved [24]. Nevertheless, the delay response of the PD cannot be measured as the spectrum analysis discarded the phase information.

In this paper, an ultrahigh-resolution optoelectronic vector analyzer (OEVA) utilizing photonics-based frequency up- and down-conversions is proposed, which features doubled frequency range and large dynamic range. In the proposed OEVA, two frequency-swept RF signals with a fixed frequency spacing

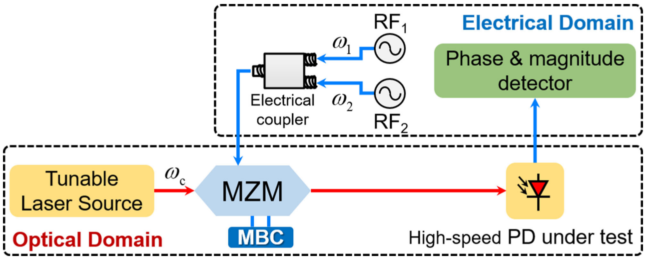

Fig. 1. Schematic configuration of the proposed OEVA. TLS, tunable laser source; PC, polarization controller; MBC, modulator bias controller; MZM, Mach-Zehnder modulator; PD, photodetector.

are used to modulate an optical carrier at a single-drive Mach-Zehnder modulator (MZM) biased at the minimum transmission point (MITP). An optical double-sideband (ODSB) signal with the suppressed optical carrier is generated and served as an optical probe signal, which is then converted into a photocurrent by the PD under test. Detecting and comparing the frequency up- and down-conversion components in the generated photocurrent, O/E frequency responses are thus obtained. In the experiment, two high-speed PDs are accurately characterized in a frequency range from 0.1 to 67 GHz by using an MZM with a 3-dB bandwidth of 25 GHz. A frequency resolution of 200 kHz is experimentally achieved. Besides, the noise performance and the dynamic range are experimentally investigated, which indicates the noise performance improves and the dynamic range enlarges with the modulation index.

II. Analytical Analysis

The schematic diagram of the configuration OEVA utilizing photonics-based frequency up- and down-conversions is shown in Fig. 1. Two RF sources produce two frequency-swept RF signals with a fixed frequency spacing, which are

$$E_{\mathrm{RF1}}(t) = V_1 \sin(\omega_1 t) \tag{1}$$

$$E_{\mathrm{RF2}}(t) = V_2 \sin(\omega_2 t + \varphi) \tag{2}$$

where V_1 and V_2 are the amplitudes of the two RF signals, respectively. ω_1 and ω_2 are the angular frequencies, which have a fixed angular frequency spacing of $\Delta\omega$ (i.e., $\Delta\omega = \omega_1 - \omega_2$) during the frequency sweeping. φ is the initial phase difference between the two RF signals. The two RF signals are combined and then modulate the optical carrier from a tunable laser source (TLS) at a single-drive MZM biased at the MITP. Hence, a carrier-suppressed ODSB signal is generated. The electrical field can be expressed as

$$\begin{aligned} &E_{\mathrm{MZM}}(t) \\ &= \frac{E_{\mathrm{c}}}{\sqrt{2}} \exp\left[i\omega_{\mathrm{c}} t + i\beta_1 \sin(\omega_1 t) + i\beta_2 \sin(\omega_2 t + \varphi) + i\pi\right] \\ &+ \frac{E_{\mathrm{c}}}{\sqrt{2}} \exp\left[i\omega_{\mathrm{c}} t + i\beta_1 \sin(\omega_1 t + \pi) + i\beta_2 \sin(\omega_2 t + \varphi + \pi)\right] \end{aligned} \tag{3}$$

where E_{c} and ω_{c} are the amplitude and angular frequency of the optical carrier, respectively. $\beta_1 = \pi V_1/V_\pi$ and $\beta_2 = \pi V_2/V_\pi$ are the modulation indices of the two RF signals, where V_π is the half-wave voltage of the MZM. Based on the Jacobi-Anger expansion, the optical signal can be rewritten as

$$\begin{aligned} E_{\mathrm{MZM}}(t) &= \frac{E_{\mathrm{c}}}{\sqrt{2}} \exp(i\omega_{\mathrm{c}} t) \\ &\times \Bigg[-\sum_{m=-\infty}^{+\infty} \sum_{n=-\infty}^{+\infty} J_m(\beta_1) J_n(\beta_2) \exp(im\omega_1 t + in\omega_2 t + in\varphi) \\ &+ \sum_{m=-\infty}^{+\infty} \sum_{n=-\infty}^{+\infty} J_m(\beta_1) J_n(\beta_2) \exp(im\omega_1 t + in\omega_2 t + in\varphi \\ &+ im\pi + in\pi) \Bigg] \end{aligned} \tag{4}$$

After square-law detection by the PD under test, a photocurrent comprising plenty of frequency components is generated. The components induced by the high-order sidebands with angular frequencies of $n\omega_1$ and $n\omega_2$ ($n = 1, 2, 3\ldots$) have no influence on the measurement results because they are frequency distinguished from the two desired components with the angular frequencies of $\omega_1 + \omega_2$ and $\omega_1 - \omega_2$. Although the components generated by the intermodulation sidebands (e.g., the third-order intermodulation (IM3) sidebands) have the same angular frequencies with the desired components, their influence is ignorable due to the very small powers. Thus, the two desired components are respectively achieved by the photonics-based frequency up- and down-conversions, which are

$$\begin{aligned} i(\omega_1 + \omega_2) = &-4R(\omega_1 + \omega_2) E_c^2 J_0(\beta_1) \\ &\times J_1(\beta_1) J_0(\beta_2) J_1(\beta_2) \exp(i\varphi) \end{aligned} \tag{5}$$

$$\begin{aligned} i(\omega_1 - \omega_2) = &4R(\omega_1 - \omega_2) E_c^2 J_0(\beta_1) J_1(\beta_1) \\ &\times J_0(\beta_2) J_1(\beta_2) \exp(-i\varphi) \end{aligned} \tag{6}$$

where $R(\omega)$ is the O/E transmission function of the PD under test. The magnitude and phase information of the desired components is extracted by an electrical phase and magnitude detector.

According to (5) and (6), the O/E transmission function can be obtained, given by

$$R(\omega_1 + \omega_2) = -\frac{i(\omega_1 + \omega_2)}{i^*(\omega_1 - \omega_2)} R^*(\omega_1 - \omega_2) \tag{7}$$

where $R^*(\omega_1 - \omega_2)$ is the conjugation of the PD's responsivity at an angular frequency of $\omega_1 - \omega_2$, which is a constant. $R(\omega_1 - \omega_2)$ is easy to measure, as the angular frequency spacing between ω_1 and ω_2 is small and fixed. In practice, a low-speed PD with the known O/E frequency response at the angular frequency of $\omega_1 - \omega_2$ can be employed to implement the frequency down-conversion.

III. Measurement Error Analysis

In practice, the limited extinction ratio (ER) and the intermodulation of the MZM inevitably lead to the residual optical carrier and the high-order intermodulation sidebands in the generated

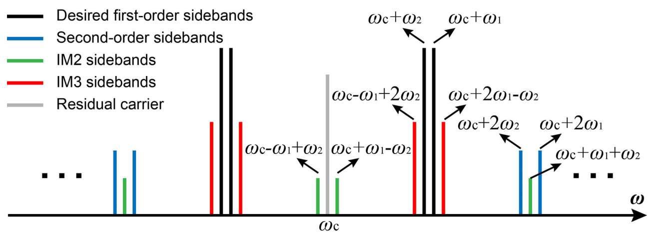

Fig. 2. The typical optical spectrum of the practically generated carrier-suppressed ODSB signal.

carrier-suppressed ODSB signal, which introduce measurement error and deteriorate the measurement accuracy. To understand the influence of these undesired sidebands, measurement error analysis is performed.

Fig. 2 shows the typical optical spectrum of the practically generated carrier-suppressed ODSB signal. Due to the weak nonlinearity, only the second-order, the IM2 and the IM3 sidebands are taken into account in the analysis. Assuming the amplitude split ratio of the Mach-Zehnder interferometer (MZI) is 1:a ($0 < a < 1$), so the ER of the MZM is

$$\mathrm{ER} = \frac{1+a^2}{1-a^2} \tag{8}$$

Hence, the frequency-domain expressions of the residual optical carrier, the desired first-order sidebands, the second-order sidebands, the IM2 sidebands and the IM3 sidebands can be written as

$$E(\omega_c) = \frac{E_c}{\sqrt{2}}(1-a)\,J_0(\beta_1)\,J_0(\beta_2) \tag{9.1}$$

$$E(\omega_c+\omega_1) = -\frac{E_c}{\sqrt{2}}(1+a)\,J_1(\beta_1)\,J_0(\beta_2) \tag{9.2}$$

$$E(\omega_c+\omega_2) = -\frac{E_c}{\sqrt{2}}(1+a)\,J_0(\beta_1)\,J_1(\beta_2)\exp(i\varphi) \tag{9.3}$$

$$E(\omega_c-\omega_2) = \frac{E_c}{\sqrt{2}}(1+a)\,J_0(\beta_1)\,J_1(\beta_2)\exp(-i\varphi) \tag{9.4}$$

$$E(\omega_c-\omega_1) = \frac{E_c}{\sqrt{2}}(1+a)\,J_1(\beta_1)\,J_0(\beta_2) \tag{9.5}$$

$$E(\omega_c+2\omega_1) = \frac{E_c}{\sqrt{2}}(1-a)\,J_2(\beta_1)\,J_0(\beta_2) \tag{9.6}$$

$$E(\omega_c+2\omega_2) = \frac{E_c}{\sqrt{2}}(1-a)\,J_0(\beta_1)\,J_2(\beta_2)\exp(i2\varphi) \tag{9.7}$$

$$E(\omega_c-2\omega_2) = \frac{E_c}{\sqrt{2}}(1-a)\,J_0(\beta_1)\,J_2(\beta_2)\exp(-i2\varphi) \tag{9.8}$$

$$E(\omega_c-2\omega_1) = \frac{E_c}{\sqrt{2}}(1-a)\,J_2(\beta_1)\,J_0(\beta_2) \tag{9.9}$$

$$E(\omega_c+\omega_1+\omega_2) = \frac{E_c}{\sqrt{2}}(1-a)\,J_1(\beta_1)\,J_1(\beta_2)\exp(i\varphi) \tag{9.10}$$

$$E(\omega_c-\omega_1-\omega_2) = \frac{E_c}{\sqrt{2}}(1-a)\,J_1(\beta_1)\,J_1(\beta_2)\exp(-i\varphi) \tag{9.11}$$

$$E(\omega_c+\omega_1-\omega_2) = -\frac{E_c}{\sqrt{2}}(1-a)\,J_1(\beta_1)\,J_1(\beta_2)\exp(-i\varphi) \tag{9.12}$$

$$E(\omega_c-\omega_1+\omega_2) = -\frac{E_c}{\sqrt{2}}(1-a)\,J_1(\beta_1)\,J_1(\beta_2)\exp(i\varphi) \tag{9.13}$$

$$E(\omega_c+2\omega_1-\omega_2) = \frac{E_c}{\sqrt{2}}(1+a)\,J_2(\beta_1)\,J_1(\beta_2)\exp(-i\varphi) \tag{9.14}$$

$$E(\omega_c-\omega_1+2\omega_2) = \frac{E_c}{\sqrt{2}}(1+a)\,J_1(\beta_1)\,J_2(\beta_2)\exp(i2\varphi) \tag{9.15}$$

$$E(\omega_c+\omega_1-2\omega_2) = -\frac{E_c}{\sqrt{2}}(1+a)\,J_1(\beta_1)\,J_2(\beta_2)\exp(-i2\varphi) \tag{9.16}$$

$$E(\omega_c-2\omega_1+\omega_2) = -\frac{E_c}{\sqrt{2}}(1+a)\,J_2(\beta_1)\,J_1(\beta_2)\exp(i\varphi) \tag{9.17}$$

According to (9.1) and (9.6) $\sim$ (9.13), the residual optical carrier, the second-order sidebands and the IM2 sidebands can be well suppressed with a large ER, as $a \to 1$ (or $1 - a \to 0$) with the increase of the ER. Additionally, the desired first-order sidebands are maximized, as can be seen from (9.2) to (9.5). But the error induced by the IM3 sidebands gets large due to the growth of the IM3 sidebands, as can be seen from (9.14) to (9.17).

To simplify the analysis, we assume that the two RF signals have the same power (e.g., $\beta = \beta_1 = \beta_2$) and the O/E transmission function of the PD under test is $R(\omega) = 1$. Thereby, the components with angular frequencies of $\omega_1 + \omega_2$ and $\omega_1 - \omega_2$ are

$$\begin{aligned} i(\omega_1+\omega_2) = &-E_c^2(1+a)^2 J_0^2(\beta)\,J_1^2(\beta)\exp(i\varphi) \\ &+E_c^2(1-a)^2 J_0^2(\beta)\,J_1^2(\beta)\exp(i\varphi) \\ &-E_c^2(1+a)^2 J_1^2(\beta)\,J_2^2(\beta)\exp(i\varphi) \end{aligned} \tag{10.1}$$

$$\begin{aligned} i(\omega_1-\omega_2) = &\,E_c^2(1+a)^2 J_0^2(\beta)\,J_1^2(\beta)\exp(-i\varphi) \\ &-E_c^2(1-a)^2 J_0(\beta)\,J_1^2(\beta)\left[J_0(\beta)-2J_2(\beta)\right]\exp(-i\varphi) \\ &-2E_c^2(1+a)^2 J_0(\beta)\,J_1^2(\beta)\,J_2(\beta)\exp(-i\varphi) \end{aligned} \tag{10.2}$$

On the right hands of (10.1) and (10.2), the first terms are the desired components generated by the first-order sidebands, while the second and third terms are the measurement error induced by the IM2 and IM3 sidebands, respectively. Since the desired components and the measurement error are in phase,

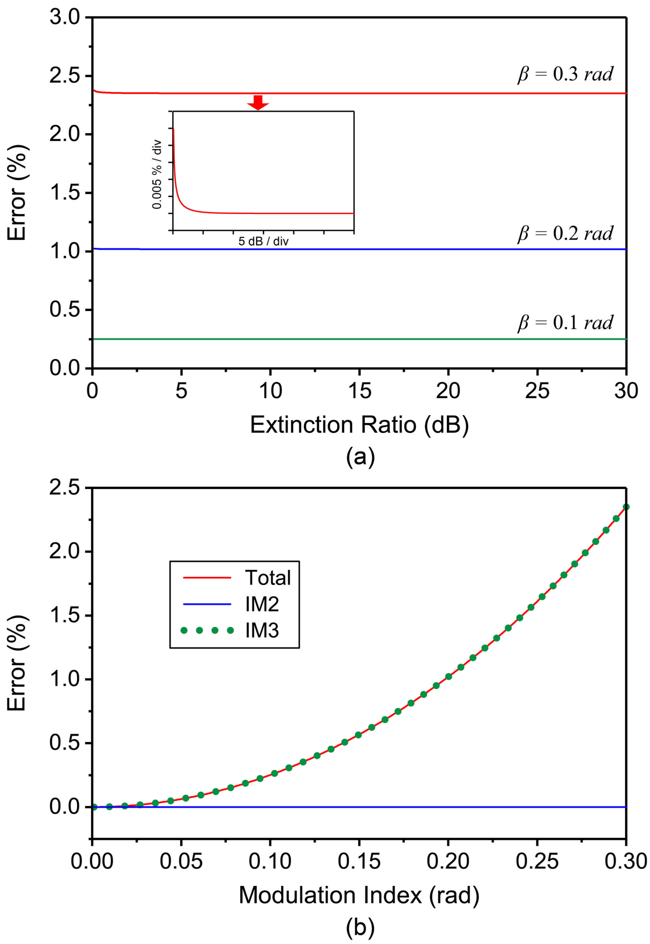

Fig. 3. (a) The measurement errors at different modulation indices and (b) the IM2-sideband-induced, IM3-sideband-induced and the total errors with an ER of 20 dB.

there is only magnitude error. It is worth noting that, the measurement error is barely introduced by the IM2 sidebands, as $(1 - a)^2 << (1 + a)^2$.

According to (10.1) and (10.2), the practically measured O/E transmission function can be achieved, which is (11) shown at the bottom of this page.

Thus, the measurement error can be expressed by (12) shown at the bottom of this page.

Fig. 3 shows the measurement errors along with the ER at different modulation indices, and the IM2-sideband-induced, the IM3-sideband-induced and the total measurement errors when the ER is set to 20 dB. As can be seen from Fig. 3(a), the measurement errors hardly change with the ER, which indicates that the residual optical carrier has an ignorable influence on the measurement since the suppression of the optical carrier is equal to ER. At a modulation index of 0.3 rad, the measurement error is only reduced by about 0.025% when the ER increases from 0.001 dB to 5dB, as shown in the inset of Fig. 3(a). With the ER beyond 5 dB, the error is unchanged. Nevertheless, the measurement error is sensitive to the modulation index. As can be seen from Fig. 3(b), the total error rapidly grows with the modulation index (red line). The IM2-sideband-introduce error (blue line) is small enough to be ignored (for example, the error is 5.71×10^{-5}% when the modulation index is 0.3 rad), while the IM3-sideband-induced error (green dot line) is coincident with the total error.

IV. Experimental Results and Discussion

An OEVA based on the schematic diagram shown in Fig. 1 is experimentally established. A compact narrow linewidth laser with a linewidth of $<$ 5 kHz (TeraXion Inc.) produces an optical carrier with a frequency of 193.533 THz. A four-port vector network analyzer (VNA, R&S ZVA67) equipped with the frequency conversion option (ZVA-K4) generates two frequency-swept RF signals with an 80-MHz frequency spacing, which are coupled and then injected into a 40-Gb/s MZM (Fujitsu FTM7937EZ) with a 3-dB electro-optic (E/O) bandwidth of 25 GHz. A modulator bias controller (MBC, YYLabs Inc.) is employed to make the MZM work at MITP. A high-speed PD (U^2T XPD2120R) with a 3-dB O/E frequency bandwidth of $\sim$50 GHz and a high-power PD (Discovery Semiconductors Inc. DSC40S) with a 3-dB O/E frequency bandwidth of $\sim$20 GHz are used as the PDs under test, respectively. The phase & magnitude detector in the VNA receives and detects the frequency up- and down-conversion components. An optical spectrum analyzer (OSA) manufactured by APEX Technologies is used to measure the optical spectrum by 5-MHz frequency resolution.

Fig. 4 shows the measured optical spectrum of the carrier-suppressed ODSB signal when two RF signals with frequencies of 10 GHz and 10.08 GHz are simultaneously applied. Since the powers of the two RF signals are set to 5 dBm, the modulation index of the MZM is correspondingly 0.21 rad. Due to the nonlinearity in the electrical-to-optical conversion, the undesired distortion sidebands, including the high-order sidebands and the

$$\begin{aligned} R_{\text{Meas.}}(\omega_1+\omega_2) &= -\frac{i(\omega_1+\omega_2)}{i^*(\omega_1-\omega_2)} \\ &= \frac{(1+a)^2 J_0^2(\beta) J_1^2(\beta) - (1-a)^2 J_0^2(\beta) J_1^2(\beta) + (1+a)^2 J_1^2(\beta) J_2^2(\beta)}{(1+a)^2 J_0^2(\beta) J_1^2(\beta) - (1-a)^2 J_0(\beta) J_1^2(\beta)\left[J_0(\beta) - 2J_2(\beta)\right] - 2(1+a)^2 J_0(\beta) J_1^2(\beta) J_2(\beta)} \end{aligned} \tag{11}$$

$$\begin{aligned} \Delta &= R_{\text{Meas.}}(\omega_1+\omega_2) - 1 \\ &= \frac{(1+a)^2 J_0^2(\beta) J_1^2(\beta) - (1-a)^2 J_0^2(\beta) J_1^2(\beta) + (1+a)^2 J_1^2(\beta) J_2^2(\beta)}{(1+a)^2 J_0^2(\beta) J_1^2(\beta) - (1-a)^2 J_0(\beta) J_1^2(\beta)\left[J_0(\beta) - 2J_2(\beta)\right] - 2(1+a)^2 J_0(\beta) J_1^2(\beta) J_2(\beta)} - 1 \end{aligned} \tag{12}$$

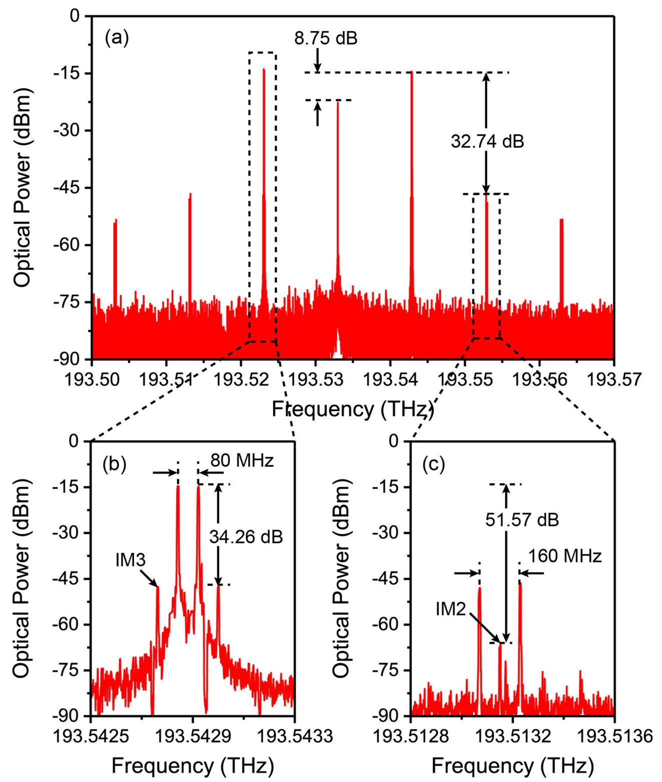

Fig. 4. (a) The measured optical spectrum of the carrier-suppressed ODSB signal achieved by modulating two RF signals with frequencies of 10 GHz and 10.08 GHz, (b) the first-order sidebands and the third-order intermodulation (IM3) sidebands, and (c) the second-order sidebands and the second-order intermodulation (IM2) sidebands.

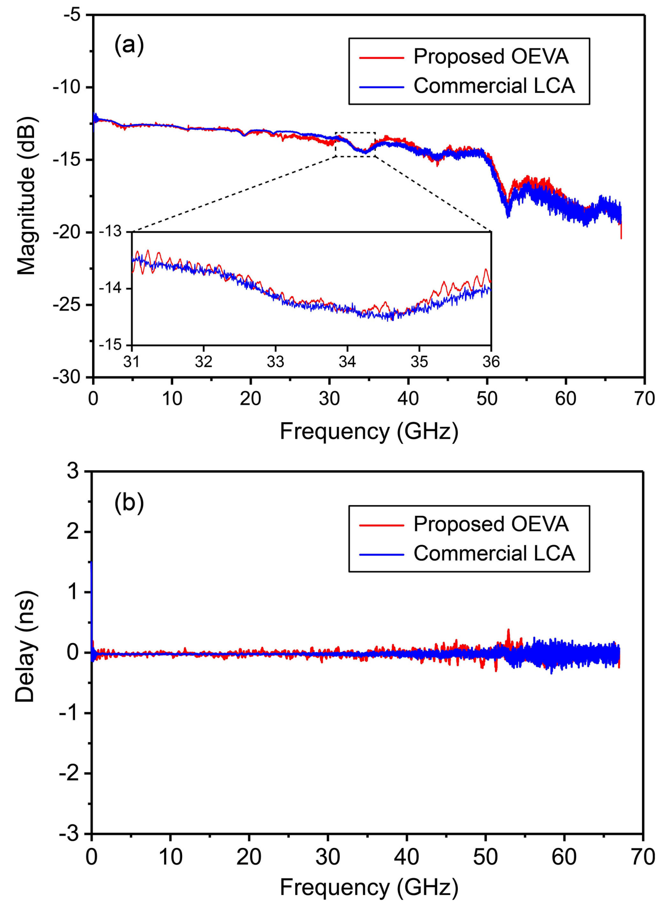

Fig. 5. The (a) magnitude and (b) delay responses of the commercial 50-GHz PD measured by the proposed OEVA and the Keysight LCA.

intermodulation sidebands, are stimulated. The powers of the high-order sidebands are much smaller than those of the desired first-order sidebands. The sideband suppression ratios (SSRs) are larger than 32.74 dB, which indicates the undesired beat notes induced by the high-order sidebands are 32.74-dB smaller than the desired components in the generated photocurrent. Moreover, the beat notes are further suppressed when receiving the desired components, as they have different frequencies from the desired components. Thus, the high-order sidebands eventually have no influence on the measurement results.

However, the intermodulation sidebands consequentially introduce the measurement error, because the components generated by the intermodulation sidebands have the same frequencies with the desired components in the photocurrent. Due to the weak intermodulation, only the IM2 sidebands and the IM3 sidebands are observed, as shown in Fig. 4(b) and (c). The IM3 sidebands appear on both sides of the first-order sidebands, while the IM2 sidebands are located in the middle of the two second-order sidebands. In the frequency down-conversion case, the intermodulation distortion is caused by the beat notes of the IM3 sidebands and the neighboring first-order sidebands, and the beat notes of the IM2 sidebands and the neighboring second-order sidebands. As can be seen from Fig. 4(b), the IM3 sidebands are 34.26-dB smaller than the desired first-order sidebands, which indicates the component beaten by the IM3 sidebands and the neighboring first-order sidebands is 34.26-dB smaller than the desired component beaten by the neighboring first-order sidebands. Consequently, the IM3 sidebands introduce $\sim$1.94% measurement error. The measurement error induced by the beat notes of the IM2 sidebands and the second-order sidebands is as small as 0.006% and ignorable, as the IM2 sidebands and the second-order sidebands are 51.57-dB and 32.74-dB smaller than the desired first-order sidebands, respectively. In the frequency up-conversion case, the measurement error is small enough to be ignored. It is because that the induced error is only 0.037% benefitting from the small powers of the IM3 sidebands, while the beat notes of the residual optical carrier and the IM2 sidebands cause 0.096% error considering that the residual optical carrier and the IM2 sidebands are 8.75-dB and 51.57-dB smaller than the desired first-order sidebands. It should be noted that the measurement error reduces with the frequency due to the decrease of the modulation index.

Fig. 5 shows the measured magnitude and delay responses of the 50-GHz PD by using the proposed OEVA and the commercial lightwave component analyzer (LCA, Keysight N4373D). As can be seen from Fig. 5(a), the O/E frequency responses (red lines) in a frequency range from 0.1 to 67 GHz are obtained by the proposed OEVA. The 3-dB O/E frequency bandwidth is recognized as 50.73 GHz, which agrees with the typical 3-dB O/E frequency bandwidth of the commercial high-speed PD. Benefitting from the ultra-fine electrical frequency sweeping, a frequency resolution up to 200 kHz is achieved according to the 334501 measurement points in the measurement range. Fig. 5(b) shows the delay response measured by the proposed OEVA after removing the delay induced by the pigtails, which is flat with the frequency.

As a comparison, the magnitude and delay responses measured by the commercial LCA (blue lines) are plotted in Fig. 5, where the frequency resolution is set to 6.7 MHz. As can be seen, the magnitude and delay responses measured by the proposed OEVA and the commercial LCA have a good coincidence. Thanks to the ultrahigh frequency resolution of the proposed OEVA, the small ripples of the O/E frequency responses are observable, as shown in the inset of Fig. 5(a). It is worth noting that, by careful comparison, some slight differences between the two measured magnitude responses can be observed. It is because the relative frequency response uncertainty of the LCA for the O/E measurement at 1550 nm is around ±0.8 dB [25] and the relative frequency response uncertainty of the proposed OEVA is about ±0.3 dB according to the measurement accuracy of the VNA.

V. Noise Performance and Dynamic Range

Although enlarging the modulation index would deteriorate the measurement accuracy, improved noise performance and enhanced dynamic range are achievable because the powers and SNRs of the desired first-order sidebands grow with the modulation index. The investigation on the noise performance and the dynamic range is experimentally performed.

Fig. 6 shows the noise performance of the measured magnitude responses when the modulation indices are respectively set to 0.07 rad, 0.12 rad, 0.21 rad, 0.29 rad, and 0.36 rad. The noise performance curves are achieved by subtracting the magnitude response measured at a modulation index of 0.41 rad from the measured magnitude responses. As can be seen, by enlarging the modulation index, the noise can be effectively suppressed, and high-performance measurement is available. Especially, the improvement of the noise performance is evident in the small modulation index cases. The great improvement of the noise performance can be clearly observed by comparing Fig. 6(a) and (b). It is worth noting that the noise performance gets worse with the RF frequency, especially when the modulation index is small, as shown in Fig. 6(a). One reason is that the E/O conversion efficiency of the MZM descends with the RF frequency. Restricted by the 3-dB E/O bandwidth of 25 GHz, the measured responses within 50 GHz have relatively good noise performance benefitting from the doubled measurement frequency range. When the frequency goes beyond 50 GHz, the noise performance deteriorates since the E/O conversion efficiency rapidly falls off beyond the working bandwidth. Another reason is the rapid decrease of the O/E conversion efficiency beyond the working bandwidth of 50 GHz, as shown in Fig. 5(a).

Fig. 7 shows the O/E frequency responses of the high-power PD measured by the proposed OEVA when the modulation indices are 0.07 rad, 0.21 rad, 0.37 rad, and 0.66 rad, respectively. As can be seen, the magnitude response of the high-power PD is accurately measured. A 3-dB O/E frequency bandwidth of

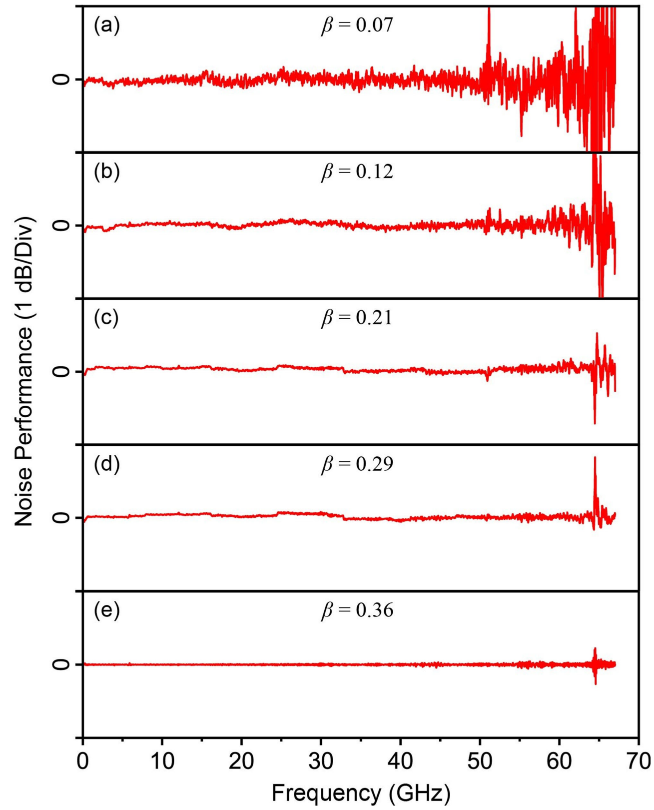

Fig. 6. The noise performance of the measured magnitude responses at different modulation indices.

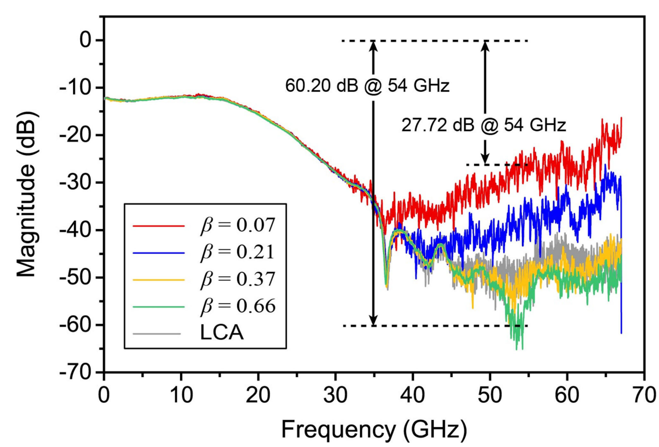

Fig. 7. The O/E frequency responses of the high-power PD measured by the proposed OEVA at different modulation indices and the commercial LCA.

20.15 GHz is recognized. In the low-frequency region (within 30 GHz), the magnitude responses measured at different modulation indices have a great coincidence and well overlapped. However, in the high-frequency region, the measured magnitude responses are obviously distinguished from each other. Benefiting from the growth of the desired first-order sidebands with the modulation index, the dynamic range of the proposed OEVA improves with the modulation index. By comparing the frequency responses measured at the modulation indices of 0.07 rad and 0.66 rad (red and green lines in Fig. 7), the dynamic range is improved from 27.72 dB to 60.20 dB around 54 GHz where the maximum notch depth is located. Hence, a dynamic range improvement of 32.48 dB is achieved by increasing the modulation index. Thanks to the large dynamic range, the fineness structure of the frequency response can be precisely observed. For instance, the sharp notch around 36.5 GHz can be precisely measured in a large dynamic range case as shown as the green line, while the notch is absent in a small dynamic range case as shown as the red line. Additionally, the dynamic range decreases with the RF frequency due to the descend of the E/O efficiency, which is demonstrated by the measured responses at the modulation indices of 0.07 rad and 0.21 rad (red and blue lines in Fig. 7). The O/E frequency response measured by the commercial LCA is also plotted for comparison as shown the grey line, which is well overlapped with the response measured when the modulation index is 0.37 rad.

It is should be noted that there is a tradeoff between the dynamic range and the measurement accuracy. The increase of the modulation index leads to the dynamic range improvement, but the measurement accuracy deteriorates by the increased measurement error induced by the IM3 sidebands, as the SSRs between the desired first-order sidebands and the undesired IM3 sidebands decrease. It is worth to mention that the dynamic range can also be enlarged by amplifying the optical testing signal using an optical amplifier before injecting the PD under test, but the noise performance would be worsened since the optical amplifier introduces additional noise in the measurement. Moreover, the dynamic range improvement is restricted by the maximum optical input power of the PD under test.

VI. Conclusion

In conclusion, an ultrahigh-resolution OEVA featuring doubled frequency range and large dynamic range is proposed to accurately characterize high-speed PDs. In the experiment, the O/E frequency responses of the two high-speed PDs from 0.1 to 67 GHz are observed by employing an MZM with a 3-dB bandwidth of 25 GHz, which agree well with the frequency responses measured by the commercial instrument. A frequency resolution as high as 200 kHz is experimentally achieved. Potentially, a sub-Hz resolution is achievable if an ultra-narrow-linewidth laser with a linewidth as narrow as sub-Hz [26] is employed and sufficient measurement points are used. The experimental investigation on the noise performance and the dynamic range shows that the increase of the modulation index improves the noise performance and enlarges the dynamic range but deteriorates the measurement accuracy. In addition, the hundred-GHz frequency range is achievable by adopting the hundred-GHz VNA and the MZM with a 3-dB bandwidth beyond 50 GHz, which are available in the market.

References

[1] J. Capmany, and D. Novak, "Microwave photonics combines two worlds," *Nature Photon.*, vol. 1, no. 6, pp. 319–330, 2007.

[2] J. Yao, "Microwave photonics," *J. Lightw. Technol.*, vol. 27, no. 3, pp. 314–335, Mar. 2009.

[3] A. J. Seeds, and K. J. Williams, "Microwave photonics," *J. Lightw. Technol.*, vol. 24, no. 12, pp. 4628–4641, Dec. 2006.

[4] R. Waterhouse, and D. Novack, "Realizing 5G: Microwave photonics for 5G mobile wireless systems," *IEEE Microw. Mag.*, vol. 16, no. 8, pp. 84–92, Sep. 2015.

[5] J. Hervás *et al.*, "Microwave photonics for optical sensors," *IEEE J. Sel. Topics Quantum Electron.*, vol. 23, no. 2, pp. 327–339, Mar.-Apr. 2017.

[6] F. Zhang *et al.*, "Photonics-based broadband radar for high-resolution and real-time inverse synthetic aperture imaging," *Opt. Express*, vol. 25, no. 14, pp. 16274–16281, 2017.

[7] H. Emami, M. Hajihashemi, S. E. Alavi, and M. Ghanbarisabagh, "Simultaneous echo power and doppler frequency measurement system based on microwave photonics technology," *IEEE Trans. Instrum. Meas.*, vol. 66, no. 3, pp. 508–513, Mar. 2017.

[8] E. Eichen, J. Schlafer, W. Rideout, and J. McCabe, "Wide-bandwidth receiver photodetector frequency response measurements using amplified spontaneous emission from a semiconductor optical amplifier," *IEEE J. Lightw. Technol.*, vol. 8, no. 6, pp. 912–916, Jun. 1990.

[9] D. M. Baney, W. V. Sorin, and S. A. Newton, "High-frequency photodiode characterization using a filtered intensity noise technique," *IEEE Photon. Technol. Lett.*, vol. 6, no. 10, pp. 1258–1260, Oct. 1994.

[10] D. F. Williams *et al.*, "Covariance-based uncertainty analysis of the NIST electrooptic sampling system," *IEEE Trans. Microw. Theory Techn.*, vol. 54, no. 1, pp. 481–491, Jan. 2006.

[11] D. R. Larson, N. G. Paulter, and D. I. Bergman, "Pulse parameter dependence on transition occurrene instant and waveform epoch," *IEEE Trans. Instrum. Meas.*, vol. 54, no. 4, pp. 1520–1526, Aug. 2005.

[12] N. G. Paulter, A. J. A. Smith, D. R. Larson, T. M. Souders, and A. G. Roddie, "NIST-NPL interlaboratory pulse measurement comparison," *IEEE Trans. Instrum. Meas.*, vol. 52, no. 6, pp. 1825–1833, Dec. 2003.

[13] D. A. Humphreys, M. Hudlicka, and I. Fatadin, "Calibration of wideband digital real-time oscilloscopes," in *Proc. Conf. Precis. Electromagn. Meas.*, Aug. 2014, pp. 698–699.

[14] D. A. Humphreys, P. M. Harris, M. Rodríguez-Higuero, F. A. Mubarak, D. Zhao, and K. Ojasalo, "Principal component compression method for covariance matrices used for uncertainty propagation," *IEEE Trans. Instrum. Meas.*, vol. 64, no. 2, pp. 356–365, Feb. 2015.

[15] T. S. Tan, R. L. Jungerman, and S. S. Elliott, "Optical receiver and modulator frequency response measurement with a Nd:YAG ring laser heterodyne technique," *IEEE Trans. Microw. Theory Techn.*, vol. 37, pp. 1217–1222, Aug. 1989.

[16] N. H. Zhu, J. M. Wen, H. S. San, H. P. Huang, L. J. Zhao, and W. Wang, "Improved optical heterodyne methods for measuring frequency responses of photodetectors," *IEEE J. Quantum Electron.*, vol. 42, no. 3, pp. 241–248, Mar. 2006.

[17] T. Dennis, and P. D. Hale, "High-accuracy photoreceiver frequency response measurements at 1.55 μm by use of a heterodyne phase-locked loop," *Opt. Express*, vol. 19, no. 21, pp. 20103–20114, 2011.

[18] N. H. Zhu, J. M. Wen, H. S. San, H. P. Huang, L. J. Zhao, and W. Wang, "Improved optical heterodyne methods for measuring frequency responses of photodetectors," *IEEE J. Quantum Electron.*, vol. 42, no. 3, pp. 241–248, Mar. 2006.

[19] B. H. Zhang *et al.*, "Development of swept frequency method for measuring frequency response of photodetectors based on harmonic analysis," *IEEE Photon. Technol. Lett.*, vol. 21, no. 7, pp. 459–461, Apr. 2009.

[20] K. Inagaki, T. Kawanishi, and M. Izutsu, "Optoelectronic frequency response measurement of photodiodes by using high-extinction ratio optical modulator," *IEICE Electron. Express*, vol. 9, no. 4, pp. 220–226, 2012.

[21] S. Zhang, C. Zhang, H. Wang, Y. Liu, J. D. Peters, and J. E. Bowers, "On-wafer probing-kit for RF characterization of silicon photonic integrated transceivers," *Opt. Express*, vol. 25, no. 12, pp. 13340–13350, 2017.

[22] S. Zhang *et al.*, "Self-calibrated microwave characterization of high-speed optoelectronic devices by heterodyne spectrum mapping," *IEEE J. Lightw. Technol.*, vol. 35, no. 10, pp. 1952–1961, May 2017.

[23] M. Yoshioka, S. Sato, and T. Kikuchi, "A method for measuring the frequency response of photodetector modules using twice-modulated light," *IEEE J. Lightw. Technol.*, vol. 23, no. 6, pp. 2112–2117, Jun. 2005.

[24] H. Wang *et al.*, "Two-tone intensity-modulated optical stimulus for self-referencing microwave characterization of high-speed photodetectors," *Opt. Commun.*, vol. 373, pp. 110–113, 2016.

[25] "Keysight N4373D lightwave component analyzer user's guide," Keysight Technologies, Manual part number 4373D-90A02, Oct. 2017. [Online]. Available: http://literature.cdn.keysight.com/litweb/pdf/4373D-90A02.pdf

[26] T. Kessler *et al.*, "A sub-40-mHz-linewidth laser based on a silicon single-crystal optical cavity," *Nature Photon.*, vol. 6, no. 10, pp. 687–692, 2012.